ISPRS Journal of Photogrammetry and Remote Sensing 154 (2019) 189–201

Contents lists available at ScienceDirect

ISPRS Journal of Photogrammetry and Remote Sensing

journal homepage: www.elsevier.com/locate/isprsjprs

Estimating leaf area index and aboveground biomass of grazing pastures using Sentinel-1, Sentinel-2 and Landsat images

Jie Wang[a], Xiangming Xiao[a,*], Rajen Bajgain[a], Patrick Starks[b], Jean Steiner[b], Russell B. Doughty[a], Qing Chang[a]

[a] Department of Microbiology and Plant Biology, Center for Spatial Analysis, University of Oklahoma, Norman, OK 73019, USA
[b] USDA-ARS Grazinglands Research Laboratory, EI Reno, OK 73036, USA

ARTICLE INFO

Keywords:
Biomass
Phenology
Vegetation indices
LAI
Remote sensing

ABSTRACT

Grassland degradation has accelerated in recent decades in response to increased climate variability and human activity. Rangeland and grassland conditions directly affect forage quality, livestock production, and regional grassland resources. In this study, we examined the potential of integrating synthetic aperture radar (SAR, Sentinel-1) and optical remote sensing (Landsat-8 and Sentinel-2) data to monitor the conditions of a native pasture and an introduced pasture in Oklahoma, USA. Leaf area index (LAI) and aboveground biomass (AGB) were used as indicators of pasture conditions under varying climate and human activities. We estimated the seasonal dynamics of LAI and AGB using Sentinel-1 (S1), Landsat-8 (LC8), and Sentinel-2 (S2) data, both individually and integrally, applying three widely used algorithms: Multiple Linear Regression (MLR), Support Vector Machine (SVM), and Random Forest (RF). Results indicated that integration of LC8 and S2 data provided sufficient data to capture the seasonal dynamics of grasslands at a 10–30-m spatial resolution and improved assessments of critical phenology stages in both pluvial and dry years. The satellite-based LAI and AGB models developed from ground measurements in 2015 reasonably predicted the seasonal dynamics and spatial heterogeneity of LAI and AGB in 2016. By comparison, the integration of S1, LC8, and S2 has the potential to improve the estimation of LAI and AGB more than 30% relative to the performance of S1 at low vegetation cover (LAI $< 2\,m^2/m^2$, AGB $< 500\,g/m^2$) and optical data of LC8 and S2 at high vegetation cover (LAI $> 2\,m^2/m^2$, AGB $> 500\,g/m^2$). These results demonstrate the potential of combining S1, LC8, and S2 monitoring grazing tallgrass prairie to provide timely and accurate data for grassland management.

1. Introduction

Grasslands are a major component of Earth's terrestrial ecosystems, covering over 30% of the global land area (Shoko et al., 2016). Grasslands provide essential ecosystem services, such as maintaining plant and animal biodiversity (Coppedge et al., 2004; WallisDeVries et al., 2002), controlling soil erosion (Talle et al., 2016), and regulating the terrestrial carbon cycle as a large carbon sink (Ali et al., 2016; Derner and Schuman, 2007; Scurlock and Hall, 1998). Furthermore, grasslands are important for livestock production, especially in areas where other agricultural enterprises are not feasible (Franzluebbers and Steiner, 2016; Steiner et al., 2014; Steiner et al., 2018). In the last several decades, grasslands have experienced degradation due to natural factors (e.g., drought, wild fires) and anthropogenic factors (e.g., overgrazing by livestock) (Le et al., 2016; Zhou et al., 2005). Additionally, grasslands are vulnerable to climate change (Cleland et al., 2006; Shoko et al., 2016) and are threatened by invasive plants (Greer et al., 2014) and woody plant encroachment (Wang et al., 2017; Wang et al., 2018). Grassland degradation negatively affects forage and livestock production and associated social-economic functions (Kwon et al., 2016). Timely information on grassland conditions is crucial for sustainable management of grassland ecosystems in the context of increased climatic variability and anthropogenic interventions (Shoko et al., 2016; Xu and Guo, 2015).

Leaf area index (LAI) and aboveground biomass (AGB) are key biophysical metrics to characterize grassland growth and conditions (Baghdadi et al., 2016; Klemas, 2013; Yu et al., 2018). LAI is an index of the photosynthetic capacity of the plant community. AGB is often used to estimate forage amount and livestock carrying capacity in grasslands (Ramoelo et al., 2015; Yang et al., 2009). LAI and AGB can be measured using ground-based methods, but these approaches are time-consuming, labor-intensive, and difficult to replicate regionally (Karimi

* Corresponding author.
E-mail address: xiangming.xiao@ou.edu (X. Xiao).

https://doi.org/10.1016/j.isprsjprs.2019.06.007
Received 29 January 2019; Received in revised form 4 June 2019; Accepted 17 June 2019

et al., 2018; Lu et al., 2016; Shoko et al., 2016). Process-based biosphere or ecosystem models can be used to simulate vegetation dynamics, including LAI and AGB of grasslands, but the results usually have coarse spatial resolutions (Foley et al., 1996; Friend et al., 1997; Haxeltine and Prentice, 1996; Tan et al., 2010). In the last few decades, remote sensing-based approaches are increasingly used to estimate LAI and AGB with a range of spatial and temporal resolutions (Yiran et al., 2012). Optical remote sensors have provided the primary data sources in these studies. Examples of these sensors (and their spatial resolutions) include the Advanced Very High Resolution Radiometer (AVHRR, ≈1-km) (Claverie et al., 2016; Jia et al., 2016), the MEdium Resolution Imaging Spectrometer (MERIS, 300-m/1200-m) (Bacour et al., 2006; Foody and Dash, 2010), the Moderate Resolution Imaging Spectroradiometer (MODIS, 250-m/500-m) (John et al., 2018; Liu et al., 2018; Myneni et al., 2002; Pasolli et al., 2015), the Landsat MSS/TM/ETM + (30-m) (Chen and Cihlar, 1996; Chen et al., 2002; Friedl et al., 1994; Turner et al., 1999; Zhang et al., 2018), the Satellite Pour l'Observation de la Terre (SPOT, 10-m/20-m) (Grant et al., 2012; Guneralp et al., 2014; Houborg et al., 2009), and other high spatial resolution satellite and airborne images (< 10-m) (Atzberger et al., 2015; Colombo et al., 2003; Darvishzadeh et al., 2011). However, optical sensor data have several limitations for estimating LAI and AGB, including: (1) the acquisition of good quality data is often constrained by weather conditions; (2) the optical data captures the information mainly from the top of canopy rather than the vegetation structure; and (3) saturation of surface reflectance and vegetation indices occurs at moderate to high vegetation cover (Chang and Shoshany, 2016; Lu, 2006). Synthetic aperture radar (SAR) sensors can penetrate clouds to acquire land surface data continuously. However, the SAR signals are affected by soil background and topography (Chang and Shoshany, 2016). Thus, integration of optical and SAR datasets would reduce the influences of soil background and weather conditions on image data analysis for grasslands (Naidoo et al., 2019). The advantages of integrated SAR and optical data were found to improve AGB estimation in non-grassland ecosystems by overcoming limitations of each sensor (Chang and Shoshany, 2016; Lu, 2006; Lu et al., 2016). Additional studies are needed to examine this integrated technology for monitoring vegetation dynamics in grazing grasslands (Svoray et al., 2013).

High spatio-temporal resolution imagery is required to inform management decisions because grasslands are highly sensitive to grazing and climate variability (Christensen et al., 2004; Thornton et al., 2014). To date, the existing LAI products (e.g. 500-m MODIS) and most herbaceous AGB estimates are in coarse or moderate spatial resolutions (Naidoo et al., 2019). The availability of Landsat-8 (LC8, 16-day revisit), Sentinel-2 (S2, 10 or 5-day revisit), and Sentinel-1 (S1, 12 or 6-day revisit) together provides time series image data at finer spatial resolutions (10-m to 30-m) and at weekly intervals, which offers an unprecedented opportunity to study grassland LAI and AGB dynamics at the field scale. It remains to: (1) assess the performance of these sensors to estimate grassland LAI and AGB within the growing season, and (2) to evaluate the improvements in comparison to the previous efforts using coarser spatial resolution and single-instrument (e.g. MODI LAI product) approaches in grazing grasslands. The LAI and AGB of grasslands have often been assessed by parametric- (e.g., Multiple linear regression models (MLR)) and non-parametric-based (e.g., support vector machines (SVM), random forest (RF)) models using ground reference data and remote sensing images (Ullah et al., 2012; Zhang et al., 2018). These models were then used to upscale ground observations to regional scales (John et al., 2018; Liang et al., 2016; Yang et al., 2018; Zhang et al., 2018). These studies have provided important basis for understanding the spatial distribution of LAI and AGB in grasslands. However, real-time or near-real time information on grassland conditions is also critically needed for supporting stakeholder and producers to make proper management decisions. The time series data from S1, LC8, and S2 favors the achievement of continuous grassland observations which is beyond the capability of previous studies that rely on less frequently obtained images.

The overall goal of this study is to explore the potential of integrating S1, LC8, and S2 data to monitor grassland (native tallgrass prairie and improved pasture) conditions at the field scale (10–30-m spatial resolution) with near weekly-interval data acquisition. The specific objectives of this study are to: (1) evaluate and understand combined time series data from S1, LC8, and S2 and the implications in tracking grassland seasonal dynamics; (2) develop LAI and AGB models based on the S1, LC8, and S2 time series data over an entire plant growing season; (3) test the potential of resultant LAI and AGB models to predict LAI and AGB in the following plant growing season; and (4) assess the potential of integrating SAR (S1) and optical remote sensing data (S2 and LC8) to monitor the spatial-temporal dynamics of LAI and AGB at the field scale.

2. Material and methods

2.1. Study sites

Our study was conducted in 2015 and 2016 at two pasture sites located at the United States Department of Agriculture (USDA) Agricultural Research Service (ARS) Grazinglands Research Laboratory (GRL), EI Reno, central Oklahoma, USA (Fig. 1). One site is a native tallgrass prairie (IGOS-E, 35.54865°N, 98.03759°W) (Bajgain et al., 2018) and the other site is an Old World bluestem (*Bothriochloa ischaemum.*) pasture (IGOS-W, 35.54679°N, 98.04529°W) (Zhou et al., 2017). Each site has an eddy covariance flux tower located within it and served as the ground reference of subsequent sampling activities.

The 1981–2010 averaged annual mean air temperature and precipitation of the study area is 5 °C and 850 mm, respectively. Year 2015 was a pluvial year with 1270 mm annual rainfall and 25% mean soil water content (SWC), which was much higher than the 635 mm annual rainfall and 22% SWC in 2016 (Fig. 1b). The soil at both sites is classed as Norge silt loam (fine, mixed, active, thermic Udic Paleustolls) with a more than 1-m depth and high water holding capacity (Fischer et al., 2012; Zhou et al., 2017). The average slope (east-facing in IGOS-E and west-facing in IGOS-W) within the flux tower footprint is about 2% at both grassland sites (Bajgain et al., 2018).

The IGOS-E site represents the native mixed grasslands of Oklahoma, dominated by big bluestem (*Andropogon gerardi* Vitman) and little bluestem (*Schizachyrium halapense (*Michx.*) Nash.*) (Bajgain et al., 2018). Since 2012, the site has been managed as part of a year-round rotational beef cow-calf (Bos Taurus) grazing system with four other rangeland pastures of similar size. This site was grazed for nine months (Jan.-Feb., Jun.-Dec.) in 2015 and six months (Jan., May-Jun., Aug.-Oct.) in 2016. Both fields were prescribed burned on 3/6/2013.

The IGOS-W site is an introduced pasture planted in Old World bluestem (*Bothriochloa ischaemum* (L) Keng). This site has received long-term management activities including burning, baling, fertilizer, herbicide, and cattle grazing (Zhou et al., 2017). Detailed management practices at this site has been summarized by Zhou et al. (2017).

2.2. Data

2.2.1. Sentinel-1 data and pre-processing

The Sentinel-1 mission has a two-satellite constellation: Sentinel-1A (S1A; launched on April 3, 2014) and Sentinel-1B (S1B; launched on April 25, 2016). The mission provides 10-m C-band SAR images with a 12- (one satellite) or 6- (two satellites) day revisit cycle. Backscatter signals are sensitive to vegetation biomass and water (Paloscia et al., 1999). The Google Earth Engine (GEE) platform has collected all the S1 data since October 2014. Each image has one- or two- polarization bands (VH, VV) at one of three resolutions: 10, 25, and 40 m. The S1 data has been processed to provide the backscatter coefficient (σ^o) in decibels (dB) using log scaling. The pre-processing includes thermal noise removal, radiometric calibration and terrain correction using

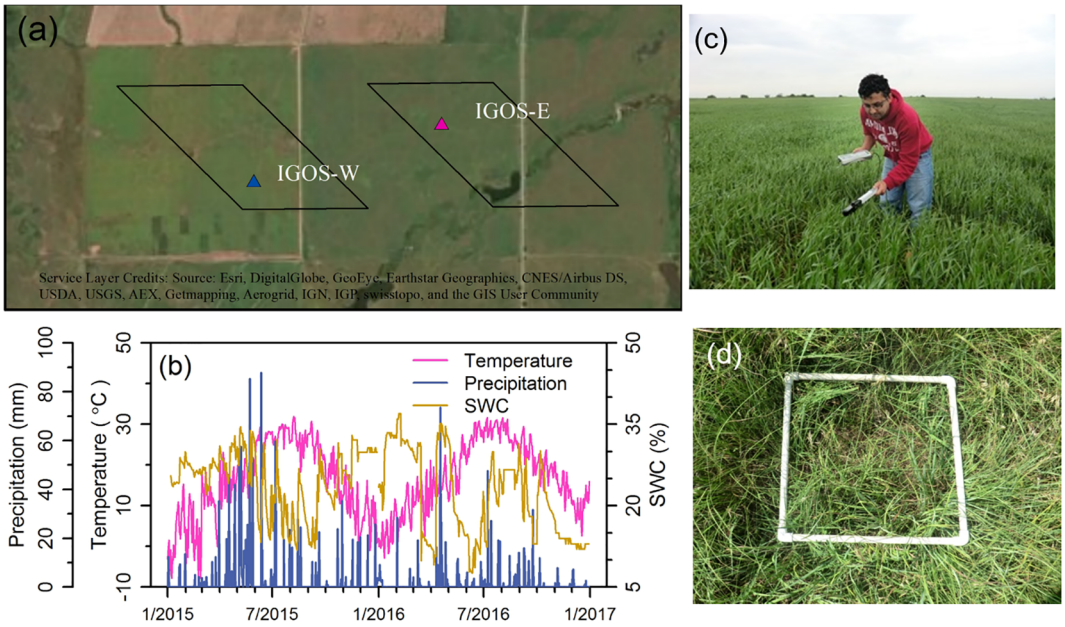

Fig. 1. (a) Locations of two grassland flux tower sites (IGOS-W and IGOS-E). The background landscape images are from world view-2 on 7/22/2016. Two black rectangles show the flux tower footprints of each site using a MODIS pixel extent according to the tower design. (b) The mean temperature, precipitation, and soil water content (SWC) of the study sites. (c, d) Pictures taken during the measurement of LAI and AGB.

Shuttle Radar Topography Mission (SRTM) 30-m or the Advanded Spaceborn Thermal Emission and Reflection Radiometer (ASTER) digital elevation model (https://developers.google.com/earth-engine/sentinel1). In this study, we used the 10-m S1 data with VH and VV polarization bands covering the study area from 01/01/2015 to 01/01/2017 for the IGOS-E and IGOS-W sites (Table S1). We generated the VV and VH time series by calculating the mean values within a 3 × 3 pixel block at each satellite visit time to match the spatial resolution of Landsat.

2.2.2. Sentinel-2 data and pre-processing

The Sentinel-2 mission also has a two-satellite constellation: Sentinel-2A (S2A, launched on June 23, 2015), and Sentinel-2B (S2B; launched on March 7, 2017). S2 carries a wide-swath multispectral imager having 13 spectral bands and a revisit time of 10- (one satellite) or 5- (two satellites) days. The spectral bands have three spatial resolutions of 10-m (Blue, Green, Red, Near Infrared (NIR) bands), 20-m (three Vegetation red edge bands, Narrow NIR band, two shortwave-infrared (SWIR) bands), and 60-m (Coastal aerosol, Water vapour, SWIR-Cirrus bands). We collected all the available S2 L1C data from June 2015 to January 2017 from the Sentinel data access hub (https://sentinel.esa.int/web/sentinel/sentinel-data-access) (Table S1). The image quality at the study sites was examined by the cloud mask band (QA60) using the GEE platform. The images at the study sites having both the opaque and cirrus cloud mask flags equal to zero (without opaque and cirrus cloud cover) were classified as good observations (Gobs), which were then processed as land surface reflectance by the atmospheric correction module (Sen2Cor) in the common Sentinel Application Platform (SNAP). Three vegetation indices (VIs) were calculated using the land surface reflectance data, Normalized Difference Vegetation Index (NDVI) (Tucker, 1979), Enhanced Vegetation Index (EVI) (Hansen et al.), and Land Surface Water Index (LSWI) (Xiao et al., 2005), to measure vegetation greenness (NDVI; EVI) and water content (LSWI). The calculation used the blue (448–546 nm), red (646–684 nm), narrow NIR (848–881 nm), and SWIR (1542–1685 nm) spectral bands.

$$NDVI = \frac{\rho_{NIR} - \rho_{red}}{\rho_{NIR} + \rho_{red}} \quad (1)$$

$$EVI = 2.5 \times \frac{\rho_{NIR} - \rho_{red}}{\rho_{NIR} + 6 \times \rho_{red} - 7.5\rho_{blue} + 1} \quad (2)$$

$$LSWI = \frac{\rho_{NIR} - \rho_{SWIR}}{\rho_{NIR} + \rho_{SWIR}} \quad (3)$$

2.2.3. Landsat-8 data and pre-processing

Landsat-8 was launched on February 11, 2013 and carries the Operational Land Imager (OLI) and the Thermal Infrared Sensor (TIRS) instruments. It provides multispectral images at 30-m resolution, with 16-day return cycle. The U.S. Geological Survey (USGS) Landsat-8 surface reflectance dataset is available from the GEE platform. The surface reflectance product was generated from the Landsat-8 Surface Reflectance Code (LaSRC), which includes atmospheric correction from TOA reflectance to surface reflectance (SR) (Vermote et al., 2016). We used all the Landsat-8 SR data from January 2015 to January 2017 (Table S1). The pixels at the study sites without bad observations (Bobs) due to clouds, cloud shadows, and snow were identified following the quality band (pixel_qa) generated from the CFmask algorithm (Zhu et al., 2015; Zhu and Woodcock, 2012). Then, these good quality surface reflectance data were used to calculate the three vegetation indices of NDVI, EVI, and LSWI (Eqs. (1)–(3)). For this sensor, the spectral bands used were blue (452–512 nm), red (636–673 nm), near-infrared (851–879 nm), and SWIR (1566–1651 nm).

2.2.4. In-situ LAI and AGB measurements

We measured the LAI (m^2/m^2) of grasslands within the IGOS-E and IGOS-W eddy covariance flux tower footprints (within a 500-m MODIS pixel) using the LAI-2200 instrument (LI-COR Biosciences, Lincoln, NE, USA). The field work was conducted bi-weekly from late March to early October in 2015 and 2016 (Table S2). Six samples were selected randomly within the footprint area of each eddy flux tower site (IGOS-E and IGOS-W). For each sample, we measured LAI three times and calculated the mean value as the final LAI at an individual sample. The final LAI at each site is the mean LAI of six samples.

On the same dates, we also collected aboveground biomass (AGB) at each study site (Table S2). AGB was measured by destructive sampling from 0.5 m^2 quadrats. At each site, we selected three quadrats within

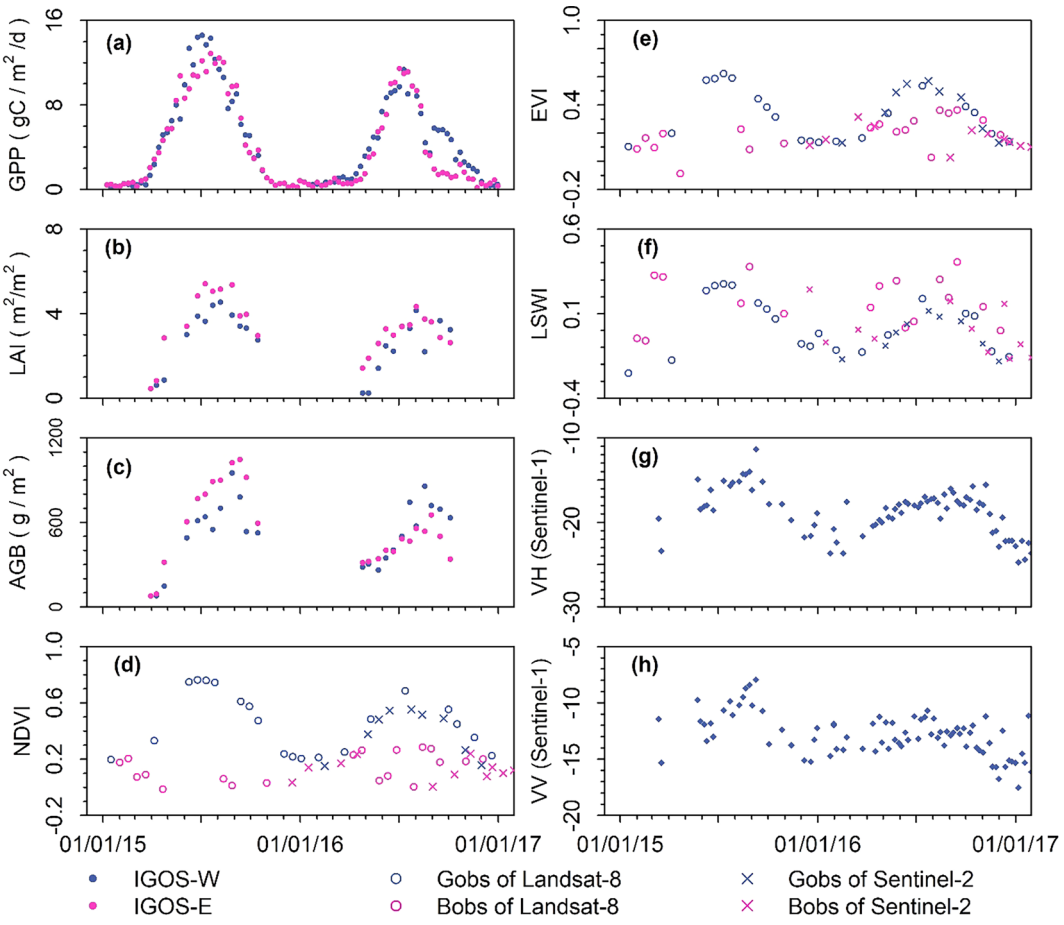

Fig. 2. (a) Gross primary production (GPP), (b) leaf area index (LAI), and (c) aboveground biomass (AGB) of IGOS-W and IGOS-E grasslands measured during 2015 and 2016. (d-h) show NDVI, EVI and LSWI and backscatters using VH and VV polarization from Landsat-8, Sentinel-2 and Sentinel-1for IGOS-E. The remote sensing observations were divided into good observations (Gobs) and bad observations (Bobs) based on the quality layer of the data (see Section 2.2.2 and 2.2.3).

the footprint of eddy flux tower and clipped all the aboveground biomass in the quadrats. The fresh samples were dried at 70 °C for 72 h and then weighed to obtain the total aboveground biomass. The AGB of each site for each date was calculated as the mean value of the total aboveground dry weight from three quadrats.

In addition, an independent AGB dataset was acquired from the IGOS-E site on July 22, 2016 (Table S2). On this date 0.5 m^2 quadrat AGB samples were collected from bottom, middle, and top of slope positions of four east-west oriented transects (thus, number of samples = 12). The slope positions within each transect were ~200 m or more away from each other, and each transect was ~200 m or more away from its nearest neighbor. Each biomass sample was clipped to within 1 cm above the soil surface, placed in a paper bag, and dried in a forced-air oven at 65 °C for 48 hrs. The dried samples were then weighed to determine dry biomass on a g m^{-2} unit. This independent AGB dataset was used to assess our model estimates in the footprint of IGOS-E tower. The footprint of the tower is shown using a 500-m MODIS pixel according to the design at tower construction. There are ten samples located in this boundary (Fig. S1).

2.2.5. MODIS-based LAI

The Collection-6 (C6) MODIS LAI and Fraction of Photosynthetically Active Radiation (FPAR) products (Myneni et al., 2015) were used for comparison with measured LAI and the output from the statistical models (described below). The C6 products have improved data quality compared to previous products due to the changes of input land cover and reflectance datasets (Wang et al., 2016; Yan et al., 2016). We used the 4-day composite Level-4 product (MCD15A3H) at 500-m pixel size. The C6 MODIS surface reflectance dataset (MOD09A1, 8-day 500-m) was also used to calculate the MODIS-based NDVI, EVI, and LSWI. The time series MODIS LAI and vegetation indices for the given pixels where IGOS-E and IGOS-W are located were constructed for the period of 01/01/2015 to 01/01/2017 using all the good-quality observations. The observation quality of MOD09A1 and MCD15A3H were from the quality bands of StateQA and FparLai_QC, respectively.

2.3. Methods

2.3.1. Seasonal dynamic analysis of vegetation indices, SAR backscatters, LAI and AGB

The seasonality of grasslands was first examined using time series LAI, AGB, and gross primary production (GPP) data from field and flux tower observations to describe the seasonal dynamics of pasture structure and function. Then, we constructed the time series of VIs (NDVI, EVI, and LSWI) from the combination of LC8 and S2, and the backscatter signals (VH, VV) from S1. These time series were analyzed to assess the ability of the satellite data to track the seasonal dynamics of grassland in LAI and AGB. In addition, we used the classic double logistic curve (Fisher et al., 2006; Zhang et al., 2003) to fit the NDVI, EVI and LSWI based on the LC8 and S2 integrated time series datasets to delineate the key phenological periods: the start of growing season (SOS), start of peak (SOP), peak of season (POS), end of peak (EOP), and end of growing season (EOS). These critical vegetation growth stages were assessed using the moving slope technique based on the VIs logistic curves (Zhang et al., 2012). SOS, EOS, SOP and EOP were identified as the transition dates defined by the extremes of second

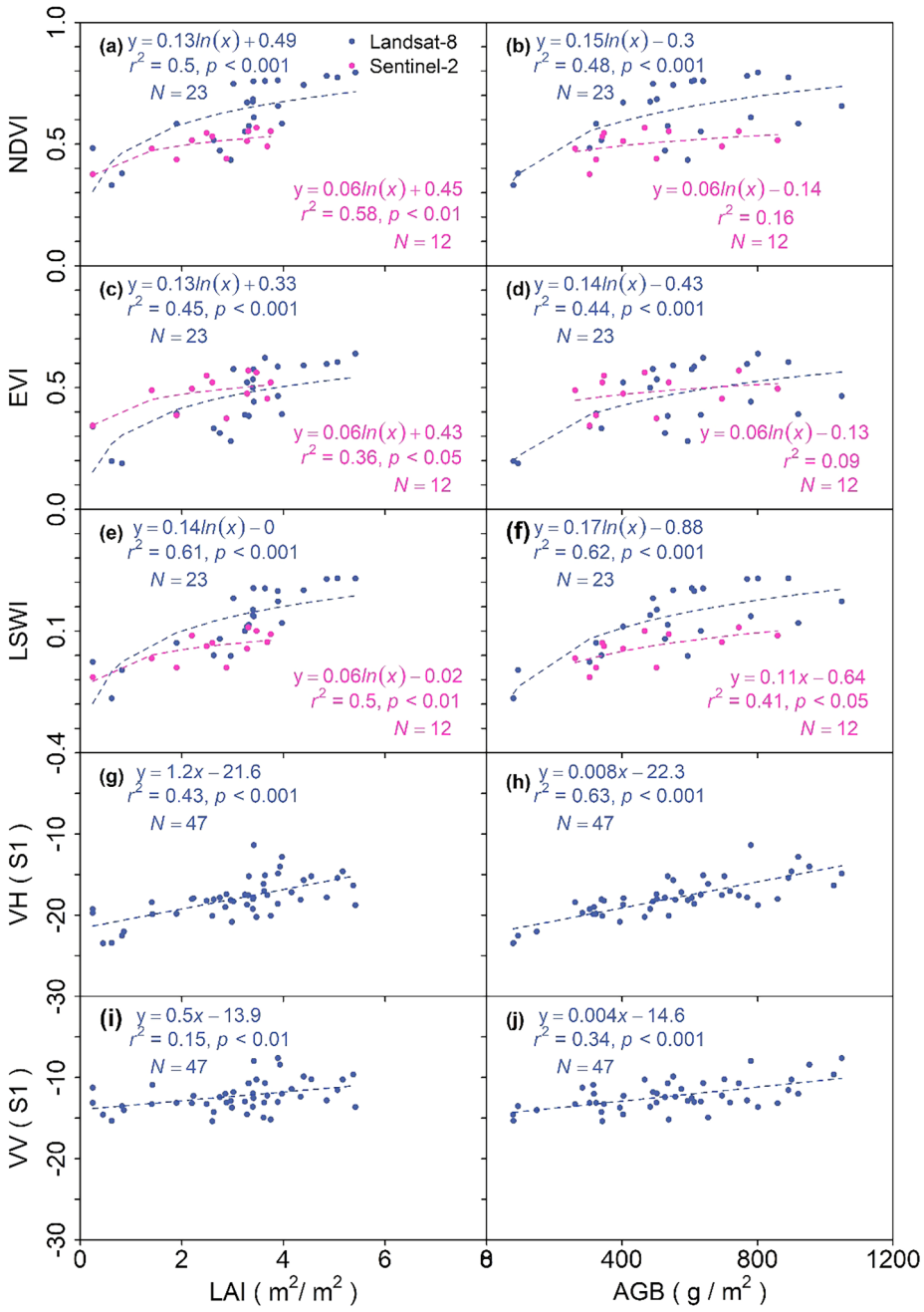

Fig. 3. Relationships between remote sensing parameters and biophysical properties: vegetation indices (NDVI, EVI and LSWI) and leaf area index (LAI) (a, c, e) and aboveground biomass (ABG) (b, d, f); backscatters (VH, VV) and LAI (g, i) and AGB (h, j).

derivatives in the simulated VIs logic curves, respectively (Gonsamo et al., 2013). POS was identified as the date with the maximum VIs values.

2.3.2. Statistical models for estimating LAI and AGB

Remote sensing variables, including backscatter signals (VV, VH) and vegetation indices (NDVI, EVI and LSWI) from S1, S2, and LC8, were used to estimate LAI and AGB using parametric (MLR) and non-parametric machine learning (SVM, RF) statistical models. The SVM and RF models were developed using R programming platform. In SVM, the input training samples are first transformed into a high-dimensional feature space using nonlinear mapping. Then, SVM performs liner regression in this feature space by minimizing training errors and model complexity. The SVM performance and application are generally controlled by the setting of hyper-parameter C, ε, and the kernel parameters (Cherkassky and Ma, 2004). In this study, we used the default value of 0.5 for ε, and the hyper-parameter C and the kernel parameter γ were optimized by the tune function to improve the assessment accuracy. RF is an ensemble approach by combining the outputs of numerous decision trees to realize the final prediction. In this study, we first created a RF model and then tuned the two parameters, number of trees (ntree) in the forest and the number of variables randomly sampled at each note (mtry), to obtain the best model (Liaw and Wiener, 2002). Detailed introductions to the applications of SVM and RF in remote sensing can be founded in Belgiu and Dragut (2016); Mountrakis et al. (2011).

To explore the potential of different datasets to track grassland dynamics, LAI and AGB models were developed using three scenarios: SAR-based models (MLR_S1, SVM_S1, and RF_S1), optical image (S2 and LC8) based models (MLR_Opt, SVM_Opt, and RF_Opt), and models

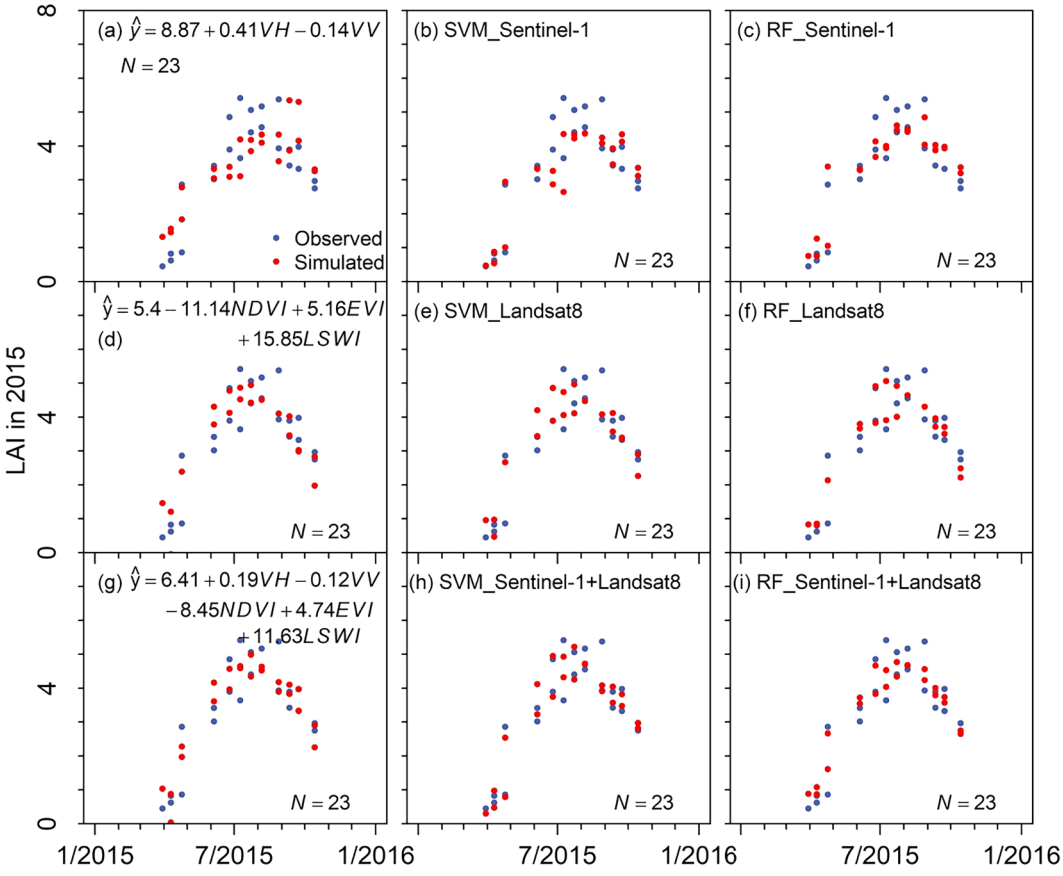

Fig. 4. Comparison of time series of model simulated leaf area index (LAI) and field observed LAI at the study sites in 2015. Multiple linear regression (MLR, a, d, g), support vector machine (SVM, b, e, h), and Random Forest (RF, c, f, i) were applied to datasets of Sentinel-1 and combination of Sentinel-1 and Landsat8 to develop the LAI models.

with the integration of both SAR and optical data (MLR_S1/Opt, SVM_S1/Opt, and RF_S1/Opt). These LAI and AGB models were developed using our ground measurements and satellite observations for 2015. The resultant LAI and AGB models were then applied to the 2016 satellite data and the results were then compared to 2016 measured LAI and AGB.

In model development and model validation, the performance of each model was evaluated using the correlation coefficient (r) and root mean squared error (RMSE):

$$r = \frac{\sum_{i=1}^{N}(P_i - \bar{P}_i)(P_m - \bar{P}_m)}{\sqrt{\sum_{i=1}^{N}(P_i - \bar{P}_i)^2 \times \sum_{i=1}^{N}(P_m - \bar{P}_m)^2}} \quad (4)$$

$$RMSE = \sqrt{\frac{1}{N}\sum_{i=1}^{N}(P_i - P_m)^2} \quad (5)$$

where P_i is the modeled LAI or AGB; P_m is the field measurement LAI or AGB; $\bar{P}_i$ is the mean of modeled results; $\bar{P}_m$ is the mean of field measurements; and N is the total number of samples.

3. Results

3.1. Seasonal dynamics of GPP, LAI, AGB, vegetation indices and SAR backscatter coefficients

Observed GPP, LAI, and AGB during 2015–2016 (Fig. 2a–c) show the seasonal dynamics of the grassland in photosynthetic activities and plant structures. The GPP, LAI, and AGB in 2015 were higher than those in 2016 with maximums of 16 g C/m^2/day, 6 m^2/m^2, and 1100 g/m^2, respectively. LAI and GPP had a similar seasonality, with the beginning to increase in late March to early April, peak values in late June to middle July, and decrease after late July. AGB started to increase during the same period as LAI and GPP but peaked in early September. After late October, GPP was very low, which indicated the end of the growing season.

To examine the capability of S1, S2, and LC8 to track the seasonality of grasslands, we analyzed the vegetation indices from the combined observations of LC8 and S2, and backscatter signals (VH, VV) of S1 (Fig. 2d–h). The VIs from the LC8 and S2 showed consistent seasonal dynamics with observed GPP and LAI (Fig. 2). The seasonality of VH and VV (Fig. 2) agreed well with that of AGB as increasing from the late March and peaking in the early September. In addition, we characterized the key phenological stages of SOS, POS, and EOS by smoothing the time series of NDVI, EVI, and LSWI using the double logistics method (Fig. S2). In general, the SOS, POS, and EOS occurred in late March to early April, late June to late July, and late September to early November, respectively.

3.2. Statistical models between in-situ LAI and vegetation indices and SAR backscatters

To establish LAI models from satellite observations, we first examined the relationships between remote sensing variables and LAI to understand the changes in satellite observations due to vegetation growth (Fig. 3). Logistic regression models showed the strongest correlations between LAI and the vegetation indices (NDVI, EVI, and LSWI) from both LC8 and S2, significant at $P < 0.01$. The correlation between LSWI and LAI was stronger than that of NDVI and EVI. A significant linear relationship was found between backscatters of S1 (VH, $R^2 = 0.43$, $P < 0.001$ and VV, $R^2 = 0.16$, $P < 0.01$) and LAI.

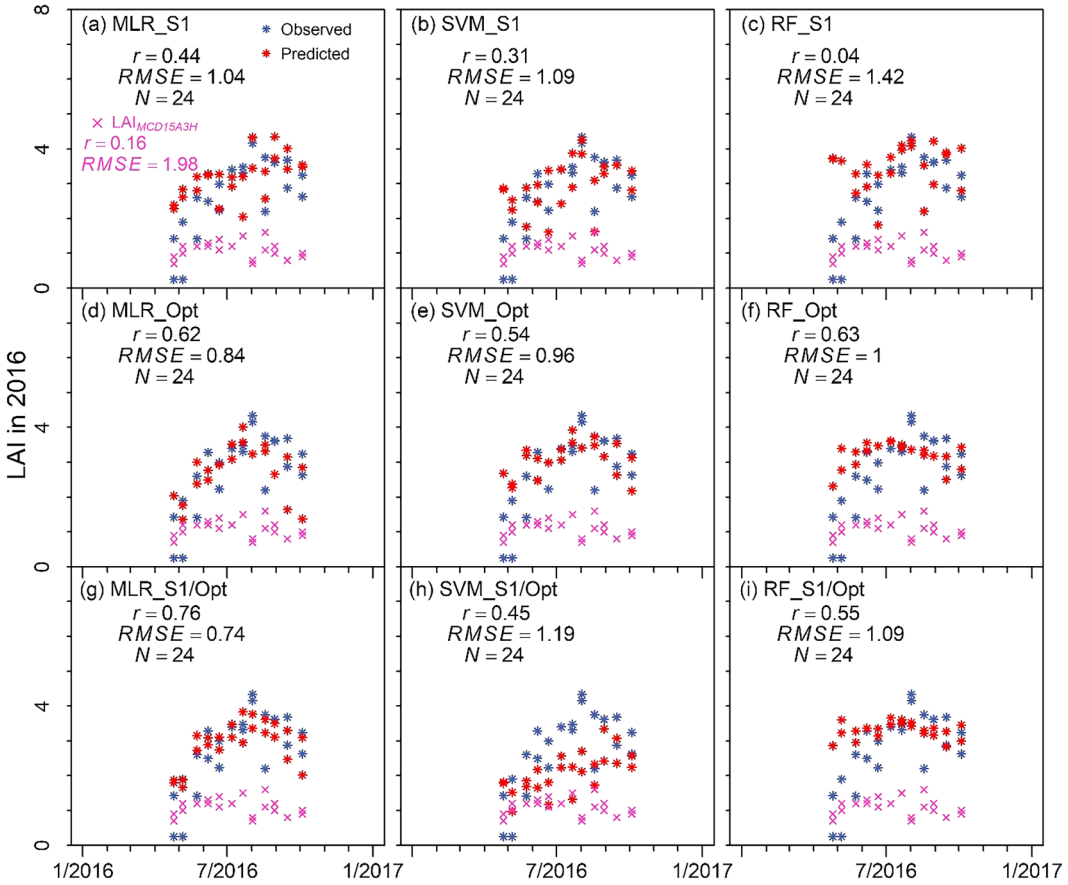

Fig. 5. Time series of model predicted leaf area index (LAI) and field observed LAI in 2016. The predicted values are obtained from three different methods multiple linear regression (MLR) at left panel, support vector machine (SVM) at middle panel, and Random Forest (RF) at right panel. These models have data inputs from three sources of Sentinel-1 (S1), Optical images (Opt) of Landsat8 and Sentinel-2, and integrated datasets (S1/Opt) of Sentinel-1, Landsat8 and Sentinel-2. This figure also shows the comparison of in-situ LAI and MODIS LAI (MCD15A3H) at the study sites in 2016 (correlation coefficient (r) and root mean squared error (RMSE) in purple). (For interpretation of the references to colour in this figure legend, the reader is referred to the web version of this article.)

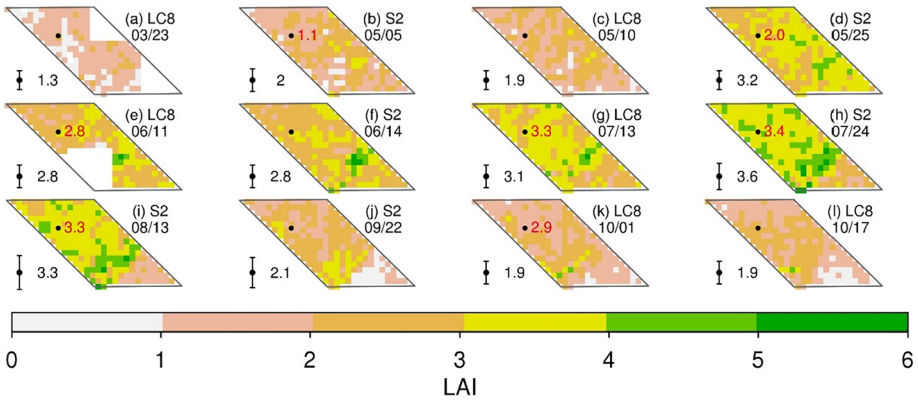

Fig. 6. Spatial and temporal dynamics of LAI in 2016 estimated by MLR_S1/Opt with 30-m spatial resolution. The mean and stand deviation within a MODIS footprint (500-m) are shown by black dots and error bars. The black dot inside the black boundary shows the location of IGOS-E. The red numbers show the measured LAI at the particular date. (For interpretation of the references to colour in this figure legend, the reader is referred to the web version of this article.)

Since the relationships between the selected variables and LAI were significant, it is possible to build remote sensing models based on these variables to predict LAI. The LAI models based on the different variables and models are shown in Fig. 4. The MLR-based models (a, d, g), SVM (b, e, h), and random forest (c, f, i) models with variables from S1, LC8, and the integration of S1 and LC8 are presented. The models were built using the field data in 2015 as training samples. The results showed that all the datasets have the potential to simulate the LAI dynamics in the growing season in 2015 (Fig. 4). Table S3 summarizes the correlation coefficients (r) and RMSE between the field measurements and the model simulations. The results also suggested that the integrated variables of S1 and LC8 produced the highest consistency between the simulations and training samples, having the highest r (0.98) and the lowest RMSE (0.27).

The resultant LAI models were used to predict the 2016 LAI dynamics (Fig. 5). The VIs from LC8 and S2 (r: 0.54–0.65, RMSE: 0.84–0.99) performed better than did S1 backscatter signals (r: 0.04–0.44, RMSE: 1.04–1.39). Among the nine models in Fig. 5, MLR based on S1, LC8, and S2 (MLR_S1/Opt) had the best performance with the highest r (0.76) and lowest RMSE (0.74).

For grazing management, we often need to monitor the spatial differences of grassland conditions. Therefore, we used the IGOS-E site

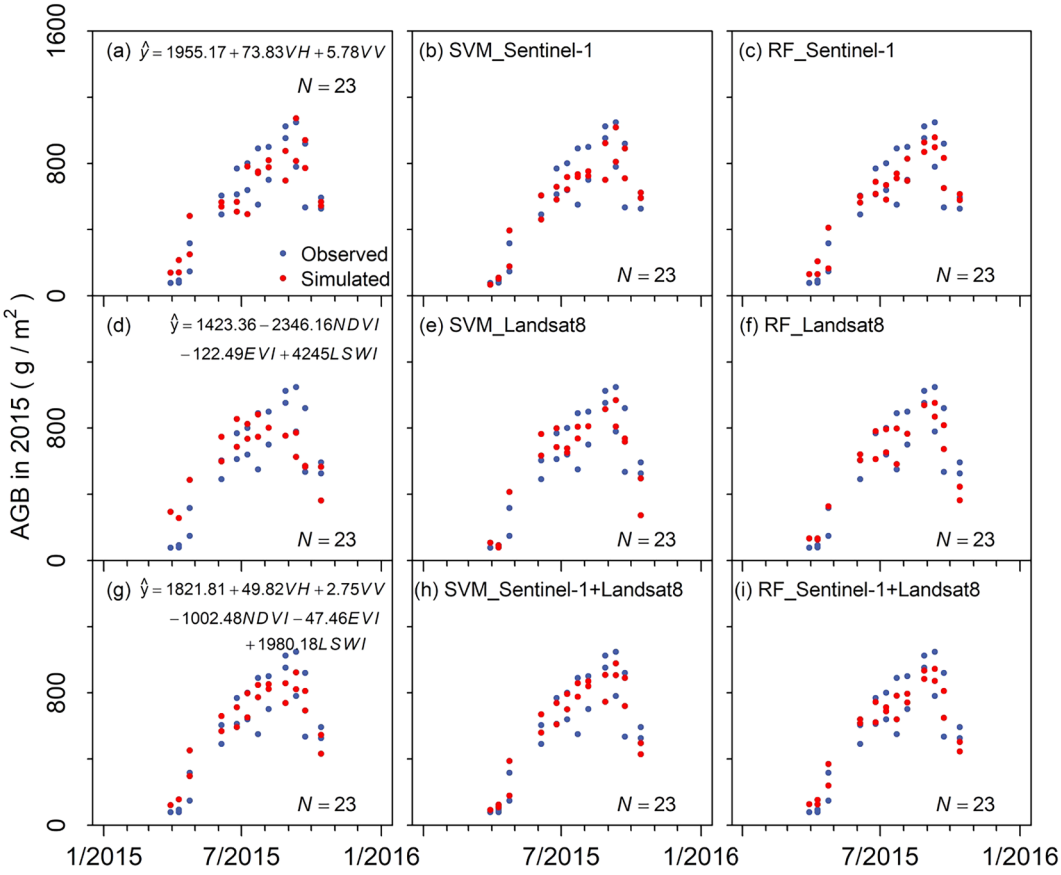

Fig. 7. Comparison of time series of model simulated aboveground biomass (AGB) and field observed AGB at the study sites in 2015. Multiple linear regression (MLR, a, d, g), support vector machine (SVM, b, e, h), and Random Forest (RF, c, f, i) were applied to datasets of Sentinel-1 and combination of Sentinel-1 and Landsat8 to develop the AGB models.

and examined the capability to monitor the spatial heterogeneity of LAI within the spatial extent of a MODIS pixel that contained the flux tower. The spatial distribution and temporal dynamics of LAI (estimated from models of MLR_S1/Opt, MLR_S1, and MLR_Opt) during the 2016 growing season are shown in Figs. 6 and S3–S4, respectively. The seasonal dynamics of LAI show increasing trend in spring, a peak in summer, and decreasing trend in fall. Spatial heterogeneity was notable in the grassland site. For example, the grasses within the right corner of the footprint had relatively low LAI (Figs. 6 and S3–S4). In comparison, S1 datasets (Fig. S3) without weather affects could provide more detail than optical data (Fig. S4) for grassland monitoring.

3.3. Statistical models between in-situ AGB and vegetation indices and backscatter

Following the same approaches used in developing the LAI models in Section 3.2, the responses of remote sensing variables to AGB increase were examined to establish the satellite-based AGB models (Fig. 3). Logistic regression models performed best in relating AGB to NDVI, EVI, and LSWI from both LC8 and S2, significant at $P < 0.05$. LSWI had a better relationship to AGB than NDVI and EVI. The linear relationship between S1 backscatter (VH, $R^2 = 0.65$ and VV, $R^2 = 0.34$) and AGB was significant ($P < 0.001$).

We used these variables from S1, LC8, and S2 to build models to predict AGB. Nine AGB models were developed based on variables from S1, LC8, and the integration of S1 and LC8 with three models of MLR (a, d, g), SVM (b, e, h) and RF (c, f, i) (Fig. 7). The results indicated good simulation of AGB dynamics in the training year (2015), having high correlations with field measurements (r: 0.79–0.98, RMSE: 87.5–181.8 g/m^2) (Fig. 7, Table S3).

The nine models show moderate to high ability to predict the AGB dynamics in 2016 with r of 0.39–0.78 and RMSE of 119.4–235.8 g/m^2 (Fig. 8). Among the nine models, MLR based on S1, LC8, and S2 (MLR_S1/Opt) provided the best performance with the r = 0.78 and RMSE of 119.4 g/m^2. In term of the MLR AGB model, the addition of VIs to VH and VV improved the model performance as indicated by higher r and lower RMSE (Fig. 8a, g). The MLR model generally performed better than SVM and RF models to predict the AGB at a site level (Fig. 8).

Figs. 9 and S5–S6 show the spatial distribution and temporal dynamics of AGB at the IGOS-E site estimated from models of MLR_S1/Opt, MLR_S1, and MLR_Opt. Like LAI, the dynamics of AGB also revealed seasonality and spatial heterogeneity in the grassland, as well as the advantage of S1 datasets providing more details on vegetation structure than optical data. The modeled AGB by MLR_S1/Opt for the tower footprint on July 24, 2016 (Fig. 9h) covers all the sample values collected on July 22, 2016 (Fig. 9m). And the statistic indicators (mean and standard deviation (SD)) of the simulated AGB are within the range of samples (Fig. 9m). Point by point analysis showed a good linear relationship between the modeled AGB and sampled AGB (Fig. 9n). Frequency analysis and liner regression were also conducted to the modeled AGB by MLR_S1 (Fig. S5ii, jj) and MLR_Opt (Fig. S6m, n). The histogram distributions and linear relationships showed that the AGB predicted by MLR_S1/Opt had a moderate mean AGB and the highest correlation with the samples, which suggested that the combination of SAR and optical data can obtain the optimal prediction.

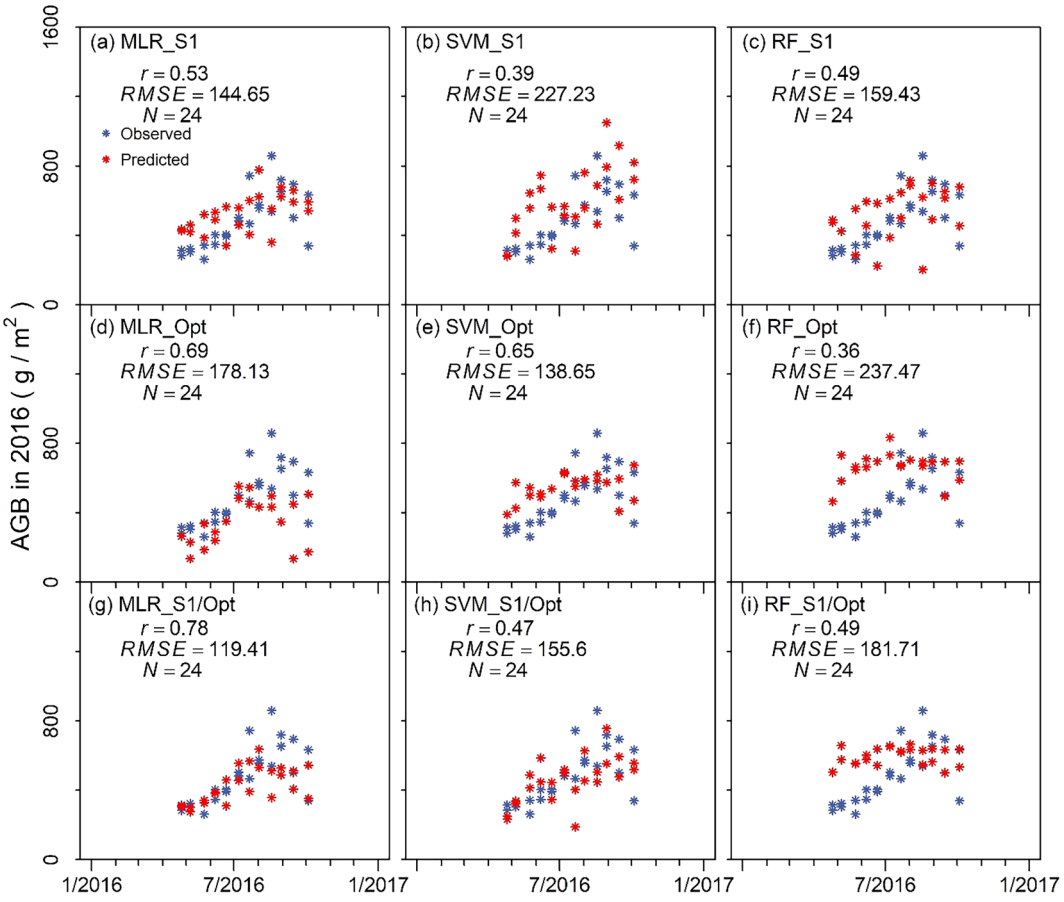

Fig. 8. Time series of model predicted aboveground biomass (AGB) and field observed AGB in 2016. The predicted values are obtained from three different methods multiple linear regression (MLR) at left panel, support vector machine (SVM) at middle panel, and Random Forest (RF) at right panel. These models have data inputs from three sources of Sentinel-1 (S1), Optical images (Opt) of Landsat8 and Sentinel-2, and integrated datasets (S1/Opt) of Sentinel-1, Landsat8 and Sentinel-2.

3.4. Inter-comparison among in-situ LAI, MODIS-based LAI and S1/S2/LC8-based LAI at the flux tower sites

Figs. 4 and 5 show that the seasonal dynamics of LAI were well simulated using S1, LC8, and S2 data, despite different accuracies (r and RMSE) among the algorithms. To understand whether these high-resolution data improved the grassland monitoring at the field scale, we also analyzed time series MODIS LAI at 500-m from MCD15A3H for comparison (Fig. 5). The comparison suggested that the MODIS LAI had a moderate correlation (r = 0.16) with field measurements. However, notable underestimates were found at these two study sites with RMSE = 1.98 m^2/m^2 (Fig. 5a). The high-resolution LAI datasets from S1, LC8, and S2 were better correlated with measured data than was the MODIS LAI at these two grassland eddy flux tower sites (r = 0.76, RMSE = 0.74 m^2/m^2 , Fig. 5g).

4. Discussion

4.1. Integration of multiple remote sensing datasets for tracking seasonal dynamics of native grasslands and pastures

The seasonal dynamics of grasslands include changes in species composition, plant community structure, and biomass production (Reed et al., 1994; Rigge et al., 2013; Smart et al., 2007), which can be used to assess livestock grazing pressure and grassland health (Rigge et al., 2013). MODIS NDVI has been widely used to describe the phenology of grasslands and pastures due to high-frequency observations (Abbas et al., 2015; Gu and Wylie, 2015; Rigge et al., 2013; Vrieling et al., 2016). However, the moderate spatial resolution (e.g., 250-m or 500-m) is often larger than the size of pastures and rangelands, and thereby captures information of surrounding land cover types (i.e., mixed pixels) (Rigge et al., 2013). In this study, we found that the VIs from LC8 and S2, in general, consistently captured the seasonality of grazing grasslands as the 500-m MODIS did (Fig. S2). We further compared the five phenology stages (SOS, SOP, POS, EOP, EOS) derived from LC8 and S2 EVI (EVI_LC8/S2), MODIS EVI (EVI_modis), and flux tower GPP to examine the capability of LC8 and S2 to delineate the physiological phenology of the grazing pastures (Fig. 10). This comparison suggested that the results from EVI_LC8/S2 (R^2, 0.92) explained more variations of phenology stages derived from GPP than EVI_modis did (R^2, 0.86) (Fig. 10c). These findings demonstrated that the combination of LC8 and S2 is promising to provide sufficient data to examine the seasonality of grasslands at a finer spatial resolution with improved tracking of key phenology stages.

S1 provides high-frequency (approximately weekly) radar images under all weather conditions (Malenovsky et al., 2012). Currently, the applications of S1 data has been largely concentrated on the aboveground biomass assessment of forests and savannas (Chang and Shoshany, 2016; Laurin et al., 2018). S1 was reported to be sensitive to the phenology dynamics of deciduous forests because leaves and upper canopy features dominate the backscatter signals in the C-band (Laurin et al., 2018). It is not fully known about the application potential to track the seasonal dynamics of grasslands. Our results found that the S1 backscatter data has the capability to track the seasonality in tallgrass prairie and pastures at the field scale (Figs. 2 and S2). It is readily applicable to study pasture and grassland under all-weather conditions in other semi-arid and sub-humid regions.

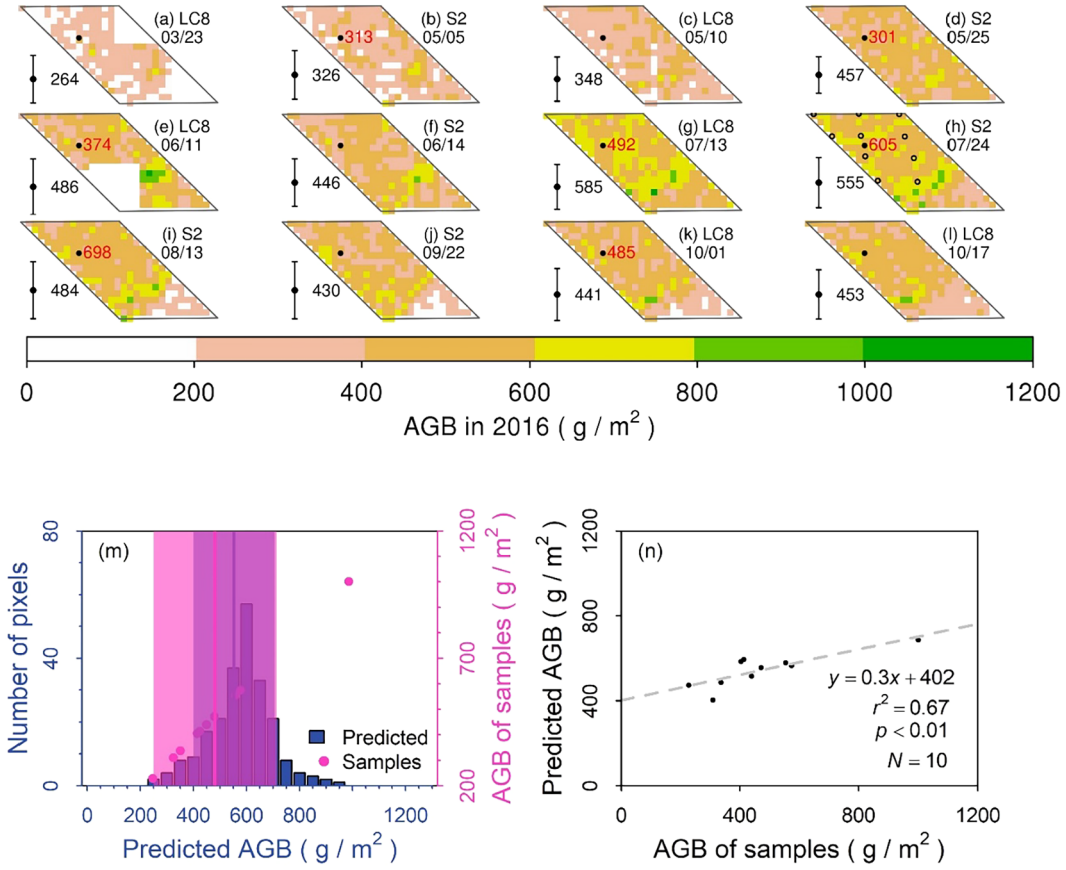

Fig. 9. Spatial and temporal dynamics of aboveground biomass (AGB) in 2016 estimated by MLR_S1/Opt with 30-m spatial resolution. The mean and stand deviation within a MODIS footprint (500-m) are shown by black dots and error bars. The black dot inside the black boundary shows the location of IGOS-E. The red numbers show the measured AGB at IGOS-E at the particular date. The points on 07/24/2016 show the distribution of ten field samples in space collected on 07/22/2016. (m) shows the histogram of predicted AGB on 07/24/2016 and pink points show the distribution of observed AGB of ten field samples. The blue line and blue shadow show the mean and standard deviation of predicted AGB. The pink line and pink shadow show the mean and standard deviation of observed AGB based on the ten field samples. (n) shows the relationship of predicted AGB and measured AGB of ten field samples in figure (h). (For interpretation of the references to colour in this figure legend, the reader is referred to the web version of this article.)

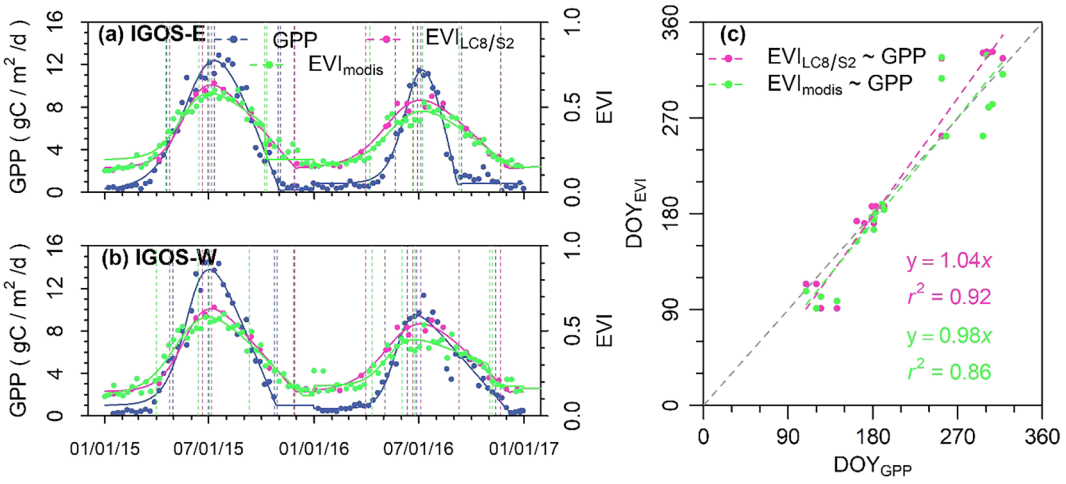

Fig. 10. (a, b) Comparisons of seasonal dynamics in flux tower GPP, LC8 and S2 EVI ($EVI_{LC8/S2}$), MODIS EVI (EVI_{modis}) at two pastures (IGOS-E and IGOS-W). The dash lines show the phenology stages (SOS, SOP, POS, EOP, and EOS) derived from GPP, $EVI_{LC8/S2}$, and EVI_{modis} time series curves. (c) Comparisons of phenology stages derived from $EVI_{LC8/S2}$ and GPP ($EVI_{LC8/S2}$ ~ GPP), and from EVI_{modis} and GPP (EVI_{modis} ~ GPP).

4.2. Estimates of grassland LAI from high resolution images (S1, S2, LC8) and moderate resolution images (MODIS)

Spectral reference and vegetation indices obtained from optical satellites are the most frequently used data to derive LAI of terrestrial ecosystems (Chen and Cihlar, 1996; Turner et al., 1999; Verrelst et al., 2012). For the grassland biome, previous efforts to assess LAI using optical data can be generalized as the applications of (1) moderate spatial resolution (greater than 100 m) remote sensing data in natural grasslands (Atzberger et al., 2015; Darvishzadeh et al., 2011;

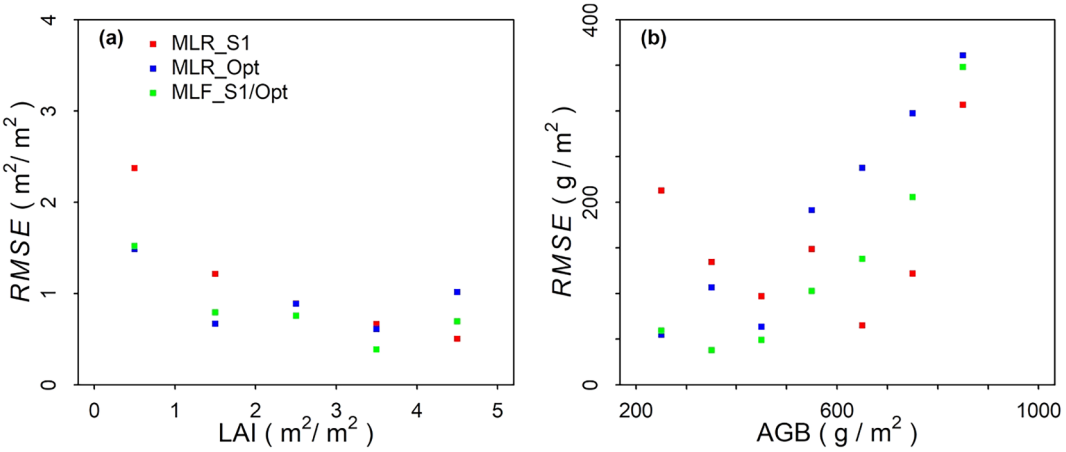

Fig. 11. RMSE at different (a) LAI and (b) AGB levels based on three data sources of SAR (MLR_S1), optical (S2 and LC8) (MLR_Opt), and the integration of SAR and optical (MLR_S1/Opt) using Multiple Linear Regression (MLR).

Darvishzadeh et al., 2008; Pasolli et al., 2015) and (2) high spatial resolution (10–100 m) satellites in grazed grasslands (Dusseux et al., 2014; Friedl et al., 1994; Li et al., 2016; Wylie et al., 2002). However, the utility of optical images for monitoring grassland dynamics during the growing seasons is usually hampered by cloud contamination and saturation at high vegetation coverage (Dusseux et al., 2014; Zhang et al., 2018). High spatial resolution S1 data could avoid these drawbacks. Thus, we compared the RMSE at different LAI levels simulated based on three data sources: SAR (MLR_S1), optical remote sensing (MLR_Opt), and the integration of SAR and optical remote sensing data (MLR_S1/Opt) (Fig. 11a). The MLR algorithm was used as example considering the good performance of MLR in this study. The prediction of LAI in 2016 from these models revealed that S1 data has the largest RMSE (e.g. RMSE is 2.4 m^2/m^2 when LAI < 1 m^2/m^2) at low vegetation coverage (LAI < 2 m^2/m^2), whereas the RMSE of optical data increased significantly when LAI was greater than 2 m^2/m^2 (e.g. RMSE is 1 m^2/m^2 when LAI > 4 m^2/m^2). This can be explained that SAR signals are susceptible to soil background at low vegetation coverage (Chang and Shoshany, 2016; Veloso et al., 2017) and optical data tends to saturation at high vegetation coverage (Huete et al., 2002). The integrated S1, S2, and LC8 data mitigated these limitations with RMSE decreased to 1.5 m^2/m^2 at LAI < 1 m^2/m^2 and to 0.69 m^2/m^2 at LAI > 4 m^2/m^2. The RMSE comparisons suggested that the integrated data was superior over S1 when LAI < 2 m^2/m^2 and superior over optical data when LAI > 2 m^2/m^2 with reducing more than 30% RMSE.

The MODIS LAI data (MCD15A3H) were significantly lower than in-situ LAI at our study sites (Fig. 5). This underestimation by MODIS LAI data product cannot be explained by the high spatial heterogeneity in the grazing grasslands and the different footprint sizes between ground measurements and MODIS observations. This finding corroborates the reports on the under- and over-estimates of MODIS LAI in grasslands and other grazing ecosystems (e.g., savannas) in previous studies (Fu and Wu, 2017; Mayr and Samimi, 2015). The S1/S2/LC8 methods developed in this paper have the potential for higher accuracy estimation of LAI at a higher spatial resolution, which would greatly increase their utility for land management applications. In addition, the LAI maps derived from S1/S2/LC8 data could also serve as a useful dataset for evaluation of MODIS LAI data product.

4.3. Estimates of grassland AGB from high resolution images (S1, S2, LC8)

Aboveground biomass assessment, mainly in natural grasslands, can be traced back to 1970s using vegetation indices from different optical satellites including AVHRR, Vegetation, MODIS, Landsat, etc. (Friedl et al., 1994; Liang et al., 2016; Shoko et al., 2016; Yang et al., 2018; Zhang et al., 2018). Previous research showed that reasonable AGB results could be obtained from these optical datasets for grassland monitoring at a low monitoring frequency (less than bi-weekly) (Gu and Wylie, 2015; John et al., 2018; Shoko et al., 2016). The C-band SAR is alternative data source for AGB assessment in grasslands, especially for regions with frequent cloud cover (Buckley and Smith, 2010; Ghasemi et al., 2011). In this study, the performances of AGB models suggest that S1 data work well to predict the AGB in grazing pastures (Fig. 8). It could surpass optical data when AGB was higher than 500 g/m^2 (Fig. 11b). The integration of S1, S2, and LC8 obtained the highest correlation coefficients (0.78) and the lowest RMSE (119.4 g/m^2) using MLR algorithm (Fig. 8). Meanwhile, the integrated data dramatically reduced the assessment errors from S1 for low AGB (< 500 g/m^2) and optical data for high AGB (> 500 g/m^2). Previous studies on AGB estimates based on S1 and S2 data are mainly conducted at forest regions (Castillo et al., 2017; Laurin et al., 2018). It is limited to understand the performance of S1 and the fusion of S1 and S2 to retrieve biomass in non-forest regions (Castillo et al., 2017). A recent publication on a grass-covered wetland reported that incorporating S1 and S2 yielded more accurate AGB estimates than did single sensors (Naidoo et al., 2019). In this study, the AGB models were built using field samples in 2015 and then assessed using the samples in 2016 (Figs. 7 and 8). In addition, we used an independent AGB field samples collected on 2016/07/22 at IGOS-E site as an auxiliary data to assess the AGB predictions from three data sources of SAR (MLR_S1), optical (S2 and LC8) (MLR_Opt), and the integrated SAR and optical (MLR_S1/Opt) data (Figs. 9, S5 and S6). MLR_S1/Opt yielded stronger linear relationship (R^2 = 0.67, P < 0.01) with the field samples than MLR_S1 (R^2 = 0.53, P = 0.01) and MLR_Opt (R^2 = 0.16, P > 0.1) did (Figs. 9, S5 and S6). Although the size of ten samples collected within the IGOS-E flux tower footprint was relatively small, it supports our finding on the higher accuracy of AGB prediction from the incorporating (MLR_S1/Opt) than the single (MLR_S1, MLR_Opt) data source. This study clearly sheds new insights for the applications of LC8, S2 and S1 on AGB studies in grazing grasslands and calls for more *in-situ* aboveground biomass samples of grasslands over space and time in the near future

5. Conclusions

Grassland conditions are threatened by several factors, such as overgrazing and droughts, which further affect the production of forage and livestock. Our study demonstrated the improvements of LC8 and S2 to capture the phenology stages, and the combination of S1, LC8, and S2 to monitor the seasonal dynamics of LAI and AGB for grazing pastures at a field scale. The timely assessments of LAI and AGB from these satellite observations are useful for estimating grazing pressure,

predicting forage production, and managing the grasslands sustainably. Our site-level study can be extended to the local or regional scale to provide information of grasslands and pastures for management, livestock production, and ecosystem service assessment.

Acknowledgments

This study was supported by research grants through the USDA National Institute of Food and Agriculture (NIFA) (2013-69002 and 2016-68002-24967) and the US National Science Foundation EPSCoR program (IIA-1301789). The field sites are operated as part of the USDA Agricultural Service Long Term Agroecosystem Research (LTAR) network. We thank two anonymous reviewers for their time and effort in reviewing the earlier version of the manuscript.

Appendix A. Supplementary material

Supplementary data to this article can be found online at https://doi.org/10.1016/j.isprsjprs.2019.06.007.

References

Abbas, S., Qamer, F.M., Murthy, M.S.R., Tripathi, N.K., Ning, W., Sharma, E., Ali, G., 2015. Grassland growth in response to climate variability in the Upper Indus Basin, Pakistan. Climate 3, 697–714.
Ali, I., Cawkwell, F., Dwyer, E., Barrett, B., Green, S., 2016. Satellite remote sensing of grasslands: from observation to management. J. Plant Ecol. 9, 649–671.
Atzberger, C., Darvishzadeh, R., Immitzer, M., Schlerf, M., Skidmore, A., le Maire, G., 2015. Comparative analysis of different retrieval methods for mapping grassland leaf area index using airborne imaging spectroscopy. Int. J. Appl. Earth Obs. 43, 19–31.
Bacour, C., Baret, F., Béal, D., Weiss, M., Pavageau, K., 2006. Neural network estimation of LAI, fAPAR, fCover and LAI×Cab, from top of canopy MERIS reflectance data: principles and validation. Remote Sens. Environ. 105, 313–325.
Baghdadi, N.N., El Hajj, M., Zribi, M., Fayad, I., 2016. Coupling SAR C-band and optical data for soil moisture and leaf area index retrieval over irrigated grasslands. Ieee J. Selected Topics Appl. Earth Observ. Remote Sensing 9, 1229–1243.
Bajgain, R., Xiao, X., Basara, J., Wagle, P., Zhou, Y., Mahan, H., Gowda, P., McCarthy, H.R., Northup, B., Neel, J., 2018. Carbon dioxide and water vapor fluxes in winter wheat and tallgrass prairie in central Oklahoma. Sci. Total Environ. 644, 1511–1524.
Belgiu, M., Dragut, L., 2016. Random forest in remote sensing: a review of applications and future directions. Isprs J. Photogramm. 114, 24–31.
Buckley, J.R., Smith, A.M., 2010. Monitoring grasslands with RADARSAT 2 quad-pol imagery. In: IEEE International Geoscience and Remote Sensing Symposium (IGARSS), 2010. IEEE, pp. 3090–3093.
Castillo, J.A.A., Apan, A.A., Maraseni, T.N., Salmo, S.G., 2017. Estimation and mapping of above-ground biomass of mangrove forests and their replacement land uses in the Philippines using Sentinel imagery. Isprs J. Photogramm. 134, 70–85.
Chang, J., Shoshany, M., 2016. Mediterranean shrublands biomass estimation using Sentinel-1 and Sentinel-2. In: 2016 IEEE International Geoscience and Remote Sensing Symposium (IGARSS), pp. 5300–5303.
Chen, J.M., Cihlar, J., 1996. Retrieving leaf area index of boreal conifer forests using landsat TM images. Remote Sens. Environ. 55, 153–162.
Chen, J.M., Pavlic, G., Brown, L., Cihlar, J., Leblanc, S.G., White, H.P., Hall, R.J., Peddle, D.R., King, D.J., Trofymow, J.A., Swift, E., Van der Sanden, J., Pellikka, P.K.E., 2002. Derivation and validation of Canada-wide coarse-resolution leaf area index maps using high-resolution satellite imagery and ground measurements. Remote Sens. Environ. 80, 165–184.
Cherkassky, V., Ma, Y.Q., 2004. Practical selection of SVM parameters and noise estimation for SVM regression. Neural Netw. 17, 113–126.
Christensen, L., Coughenour, M.B., Ellis, J.E., Chen, Z.Z., 2004. Vulnerability of the Asian typical steppe to grazing and climate change. Clim. Change 63, 351–368.
Claverie, M., Matthews, J., Vermote, E., Justice, C., 2016. A 30+ Year AVHRR LAI and FAPAR climate data record: algorithm description and validation. Remote Sens.-Basel 8, 263.
Cleland, E.E., Chiariello, N.R., Loarie, S.R., Mooney, H.A., Field, C.B., 2006. Diverse responses of phenology to global changes in a grassland ecosystem. Proc. Natl. Acad. Sci. USA 103, 13740–13744.
Colombo, R., Bellingeri, D., Fasolini, D., Marino, C.M., 2003. Retrieval of leaf area index in different vegetation types using high resolution satellite data. Remote Sens. Environ. 86, 120–131.
Coppedge, B.R., Engle, D.M., Masters, R.E., Gregory, M.S., 2004. Predicting juniper encroachment and CRP effects on avian community dynamics in southern mixed-grass prairie. USA. Biol. Conserv. 115, 431–441.
Darvishzadeh, R., Atzberger, C., Skidmore, A., Schlerf, M., 2011. Mapping grassland leaf area index with airborne hyperspectral imagery: a comparison study of statistical approaches and inversion of radiative transfer models. Isprs J. Photogramm. 66, 894–906.
Darvishzadeh, R., Skidmore, A., Schlerf, M., Atzberger, C., 2008. Inversion of a radiative transfer model for estimating vegetation LAI and chlorophyll in a heterogeneous grassland. Remote Sens. Environ. 112, 2592–2604.
Derner, J.D., Schuman, G.E., 2007. Carbon sequestration and rangelands: a synthesis of land management and precipitation effects. J. Soil Water Conserv. 62, 77–85.
Dusseux, P., Corpetti, T., Hubert-Moy, L., Corgne, S., 2014. Combined use of multi-temporal optical and radar satellite images for grassland monitoring. Remote Sens.-Basel 6, 6163–6182.
Fischer, M.L., Torn, M.S., Billesbach, D.P., Doyle, G., Northup, B., Biraud, S.C., 2012. Carbon, water, and heat flux responses to experimental burning and drought in a tallgrass prairie. Agric. For. Meteorol. 166, 169–174.
Fisher, J.I., Mustard, J.F., Vadeboncoeur, M.A., 2006. Green leaf phenology at Landsat resolution: scaling from the field to the satellite. Remote Sens. Environ. 100, 265–279.
Foley, J.A., Prentice, I.C., Ramankutty, N., Levis, S., Pollard, D., Sitch, S., Haxeltine, A., 1996. An integrated biosphere model of land surface processes, terrestrial carbon balance, and vegetation dynamics. Global Biogeochem. Cycles 10, 603–628.
Foody, G.M., Dash, J., 2010. Estimating the relative abundance of C3 and C4 grasses in the Great Plains from multi-temporal MTCI data: issues of compositing period and spatial generalizability. Int. J. Remote Sens. 31, 351–362.
Franzluebbers, A.J., Steiner, J.L., 2016. Briefing Note 34.1 Ecosystem services and grasslands in America. Routledge Handbook of Ecosystem Services, 436.
Friedl, M.A., Michaelsen, J., Davis, F.W., Walker, H., Schimel, D.S., 1994. Estimating Grassland Biomass and Leaf-Area Index Using Ground and Satellite Data. Int. J. Remote Sens. 15, 1401–1420.
Friend, A.D., Stevens, A.K., Knox, R.G., Cannell, M.G.R., 1997. A process-based, terrestrial biosphere model of ecosystem dynamics (Hybrid v3.0). Ecol. Model. 95, 249–287.
Fu, G., Wu, J.S., 2017. Validation of MODIS collection 6 FPAR/LAI in the alpine grassland of the Northern Tibetan Plateau. Remote Sens. Lett. 8, 831–838.
Ghasemi, N., Sahebi, M.R., Mohammadzadeh, A., 2011. A review on biomass estimation methods using synthetic aperture radar data. Int. J. Geomatics Geosci. 1, 776.
Gonsamo, A., Chen, J.M., D'Odorico, P., 2013. Deriving land surface phenology indicators from CO_2 eddy covariance measurements. Ecol. Indic. 29, 203–207.
Grant, K.M., Johnson, D.L., Hildebrand, D.V., Peddle, D.R., 2012. Quantifying biomass production on rangeland in southern Alberta using SPOT imagery. Canadian J. Remote Sensing 38, 695–708.
Greer, M.J., Wilson, G.W.T., Hickman, K.R., Wilson, S.M., 2014. Experimental evidence that invasive grasses use allelopathic biochemicals as a potential mechanism for invasion: chemical warfare in nature. Plant Soil 385, 165–179.
Gu, Y.X., Wylie, B.K., 2015. Developing a 30-m grassland productivity estimation map for central Nebraska using 250-m MODIS and 30-m Landsat-8 observations. Remote Sens. Environ. 171, 291–298.
Guneralp, I., Filippi, A.M., Randall, J., 2014. Estimation of floodplain aboveground biomass using multispectral remote sensing and nonparametric modeling. Int. J. Appl. Earth Obs. 33, 119–126.
Hansen, M.C., Potapov, P.V., Goetz, S.J., Turubanova, S., Tyukavina, A., Krylov, A., Kommareddy, A., Egorov, A., Mapping tree height distributions in Sub-Saharan Africa using Landsat 7 and 8 data. Remote Sens. Environ.
Haxeltine, A., Prentice, I.C., 1996. BIOME3: an equilibrium terrestrial biosphere model based on ecophysiological constraints, resource availability, and competition among plant functional types. Global Biogeochem. Cycles 10, 693–709.
Houborg, R., Anderson, M., Daughtry, C., 2009. Utility of an image-based canopy reflectance modeling tool for remote estimation of LAI and leaf chlorophyll content at the field scale. Remote Sens. Environ. 113, 259–274.
Huete, A., Didan, K., Miura, T., Rodriguez, E.P., Gao, X., Ferreira, L.G., 2002. Overview of the radiometric and biophysical performance of the MODIS vegetation indices. Remote Sens. Environ. 83, 195–213.
Jia, W.X., Liu, M., Yang, Y.H., He, H.L., Zhu, X.D., Yang, F., Yin, C., Xiang, W.N., 2016. Estimation and uncertainty analyses of grassland biomass in Northern China: comparison of multiple remote sensing data sources and modeling approaches. Ecol. Indic. 60, 1031–1040.
John, R., Chen, J., Giannico, V., Park, H., Xiao, J., Shirkey, G., Ouyang, Z., Shao, C., Lafortezza, R., Qi, J., 2018. Grassland canopy cover and aboveground biomass in Mongolia and Inner Mongolia: spatiotemporal estimates and controlling factors. Remote Sens. Environ. 213, 34–48.
Karimi, S., Sadraddini, A.A., Nazemi, A.H., Xu, T.R., Fard, A.F., 2018. Generalizability of gene expression programming and random forest methodologies in estimating cropland and grassland leaf area index. Comput. Electron. Agric. 144, 232–240.
Klemas, V., 2013. Remote sensing of coastal wetland biomass: an overview. J. Coast. Res. 29, 1016–1028.
Kwon, H.-Y., Nkonya, E., Johnson, T., Graw, V., Kato, E., Kihiu, E., 2016. Global estimates of the impacts of grassland degradation on livestock productivity from 2001 to 2011. In: Nkonya, E., Mirzabaev, A., von Braun, J. (Eds.), Economics of Land Degradation and Improvement – A Global Assessment for Sustainable Development. Springer International Publishing, Cham, pp. 197–214.
Laurin, G.V., Balling, J., Corona, P., Mattioli, W., Papale, D., Puletti, N., Rizzo, M., Truckenbrodt, J., Urban, M., 2018. Above-ground biomass prediction by Sentinel-1 multitemporal data in central Italy with integration of ALOS2 and Sentinel-2 data. J. Appl. Remote Sensing 12.
Le, Q.B., Nkonya, E., Mirzabaev, A., 2016. Biomass productivity-based mapping of global land degradation hotspots. In: Nkonya, E., Mirzabaev, A., von Braun, J. (Eds.), Economics of Land Degradation and Improvement – A Global Assessment for Sustainable Development. Springer International Publishing, Cham, pp. 55–84.
Li, Z.W., Wang, J.H., Tang, H., Huang, C.Q., Yang, F., Chen, B.R., Wang, X., Xin, X.P., Ge, Y., 2016. Predicting grassland leaf area index in the meadow steppes of Northern China: a comparative study of regression approaches and hybrid geostatistical methods. Remote Sens.-Basel 8.
Liang, T.G., Yang, S.X., Feng, Q.S., Liu, B.K., Zhang, R.P., Huang, X.D., Xie, H.J., 2016.

Multi-factor modeling of above-ground biomass in alpine grassland: a case study in the Three-River Headwaters Region, China. Remote Sens. Environ. 186, 164–172.
Liaw, A., Wiener, M., 2002. Classification and regression by randomForest. R news 2, 18–22.
Liu, Y.B., Xiao, J.F., Ju, W.M., Zhu, G.L., Wu, X.C., Fan, W.L., Li, D.Q., Zhou, Y.L., 2018. Satellite-derived LAI products exhibit large discrepancies and can lead to substantial uncertainty in simulated carbon and water fluxes. Remote Sens. Environ. 206, 174–188.
Lu, D.S., 2006. The potential and challenge of remote sensing-based biomass estimation. Int. J. Remote Sens. 27, 1297–1328.
Lu, D.S., Chen, Q., Wang, G.X., Liu, L.J., Li, G.Y., Moran, E., 2016. A survey of remote sensing-based aboveground biomass estimation methods in forest ecosystems. Int. J. Digital Earth 9, 63–105.
Malenovsky, Z., Rott, H., Cihlar, J., Schaepman, M.E., Garcia-Santos, G., Fernandes, R., Berger, M., 2012. Sentinels for science: potential of Sentinel-1, -2, and -3 missions for scientific observations of ocean, cryosphere, and land. Remote Sens. Environ. 120, 91–101.
Mayr, M.J., Samimi, C., 2015. Comparing the dry season in-situ leaf area index (LAI) derived from high-resolution RapidEye imagery with MODIS LAI in a Namibian Savanna. Remote Sens.-Basel 7, 4834–4857.
Mountrakis, G., Im, J., Ogole, C., 2011. Support vector machines in remote sensing: a review. Isprs J. Photogramm. 66, 247–259.
Myneni, R., Knyazikhin, Y., Park, T., 2015. MOD15A2H MODIS Leaf Area Index/FPAR 8-Day L4 Global 500m SIN Grid V006. NASA EOSDIS Land Processes DAAC.
Myneni, R.B., Hoffman, S., Knyazikhin, Y., Privette, J.L., Glassy, J., Tian, Y., Wang, Y., Song, X., Zhang, Y., Smith, G.R., Lotsch, A., Friedl, M., Morisette, J.T., Votava, P., Nemani, R.R., Running, S.W., 2002. Global products of vegetation leaf area and fraction absorbed PAR from year one of MODIS data. Remote Sens. Environ. 83, 214–231.
Naidoo, L., van Deventer, H., Ramoelo, A., Mathieu, R., Nondlazi, B., Gangat, R., 2019. Estimating above ground biomass as an indicator of carbon storage in vegetated wetlands of the grassland biome of South Africa. Int. J. Appl. Earth Obs. 78, 118–129.
Paloscia, S., Macelloni, G., Pampaloni, P., Sigismondi, S., 1999. The potential of C- and L-band SAR in estimating vegetation biomass: the ERS-1 and JERS-1 experiments. Ieee Trans. Geosci. Remote Sensing 37, 2107–2110.
Pasolli, L., Asam, S., Castelli, M., Bruzzone, L., Wohlfahrt, G., Zebisch, M., Notarnicola, C., 2015. Retrieval of Leaf Area Index in mountain grasslands in the Alps from MODIS satellite imagery. Remote Sens. Environ. 165, 159–174.
Ramoelo, A., Cho, M.A., Mathieu, R., Madonsela, S., van de Kerchove, R., Kaszta, Z., Wolff, E., 2015. Monitoring grass nutrients and biomass as indicators of rangeland quality and quantity using random forest modelling and World View-2 data. Int. J. Appl. Earth Obs. 43, 43–54.
Reed, B.C., Brown, J.F., Vanderzee, D., Loveland, T.R., Merchant, J.W., Ohlen, D.O., 1994. Measuring phenological variability from satellite imagery. J. Veg. Sci. 5, 703–714.
Rigge, M., Smart, A., Wylie, B., Gilmanov, T., Johnson, P., 2013. Linking phenology and biomass productivity in South Dakota mixed-grass prairie. Rangeland Ecol. Manag. 66, 579–587.
Scurlock, J.M.O., Hall, D.O., 1998. The global carbon sink: a grassland perspective. Global Change Biol. 4, 229–233.
Shoko, C., Mutanga, O., Dube, T., 2016. Progress in the remote sensing of C3 and C4 grass species aboveground biomass over time and space. Isprs J. Photogramm. 120, 13–24.
Smart, A.J., Dunn, B.H., Johnson, P.S., Xu, L., Gates, R.N., 2007. Using weather data to explain herbage yield on three great plains plant communities. Rangeland Ecol. Manag. 60, 146–153.
Steiner, J.L., Franzluebbers, A.J., Neely, C., Ellis, T., Aynekulu, E., 2014. Enhancing soil and landscape quality in smallholder grazing systems. Soil Management of Smallholder Agriculture. Adv. Soil Sci. 63–111.
Steiner, J.L., Wagle, P., Gowda, P., Lands, G., 2018. Management of water resources for grasslands Research Laboratory–USDA-ARS, USA, Improving grassland and pasture management in temperate agriculture. Burleigh Dodds Science Publishing, pp. 285–302.
Svoray, T., Perevolotsky, A., Atkinson, P.M., 2013. Ecological sustainability in rangelands: the contribution of remote sensing. Int. J. Remote Sens. 34, 6216–6242.
Talle, M., Deak, B., Poschlod, P., Valko, O., Westerberg, L., Milberg, P., 2016. Grazing vs. mowing: a meta-analysis of biodiversity benefits for grassland management. Agric. Ecosyst. Environ. 222, 200–212.
Tan, K., Ciais, P., Piao, S.L., Wu, X.P., Tang, Y.H., Vuichard, N., Liang, S., Fang, J.Y., 2010. Application of the ORCHIDEE global vegetation model to evaluate biomass and soil carbon stocks of Qinghai-Tibetan grasslands. Global Biogeochem. Cycles 24.
Thornton, P.K., Ericksen, P.J., Herrero, M., Challinor, A.J., 2014. Climate variability and vulnerability to climate change: a review. Global Change Biology 20, 3313–3328.
Tucker, C.J., 1979. Red and photographic infrared linear combinations for monitoring vegetation. Remote Sens. Environ. 8, 127–150.
Turner, D.P., Cohen, W.B., Kennedy, R.E., Fassnacht, K.S., Briggs, J.M., 1999. Relationships between leaf area index and Landsat TM spectral vegetation indices across three temperate zone sites. Remote Sens. Environ. 70, 52–68.
Ullah, S., Si, Y., Schlerf, M., Skidmore, A.K., Shafique, M., Iqbal, I.A., 2012. Estimation of grassland biomass and nitrogen using MERIS data. Int. J. Appl. Earth Obs. 19, 196–204.
Veloso, A., Mermoz, S., Bouvet, A., Toan, T.L., Planells, M., Dejoux, J.F., Ceschia, E., 2017. Understanding the temporal behavior of crops using Sentinel-1 and Sentinel-2-like data for agricultural applications. Remote Sens. Environ. 199, 415–426.
Vermote, E., Justice, C., Claverie, M., Franch, B., 2016. Preliminary analysis of the performance of the Landsat 8/OLI land surface reflectance product. Remote Sens. Environ. 185, 46–56.
Verrelst, J., Munoz, J., Alonso, L., Delegido, J., Rivera, J.P., Camps-Valls, G., Moreno, J., 2012. Machine learning regression algorithms for biophysical parameter retrieval: opportunities for Sentinel-2 and -3. Remote Sens. Environ. 118, 127–139.
Vrieling, A., Meroni, M., Mude, A.G., Chantarat, S., Ummenhofer, C.C., de Bie, K., 2016. Early assessment of seasonal forage availability for mitigating the impact of drought on East African pastoralists. Remote Sens. Environ. 174, 44–55.
WallisDeVries, M.F., Poschlod, P., Willems, J.H., 2002. Challenges for the conservation of calcareous grasslands in northwestern Europe: integrating the requirements of flora and fauna. Biol. Conserv. 104, 265–273.
Wang, C., Feng, M.-C., Yang, W.-D., Ding, G.-W., Sun, H., Liang, Z.-Y., Xie, Y.-K., Qiao, X.-X., 2016. Impact of spectral saturation on leaf area index and aboveground biomass estimation of winter wheat. Spectrosc. Lett. 49, 241–248.
Wang, J., Xiao, X., Qin, Y., Dong, J., Geissler, G., Zhang, G., Cejda, N., Alikhani, B., Doughty, R.B., 2017. Mapping the dynamics of eastern redcedar encroachment into grasslands during 1984–2010 through PALSAR and time series Landsat images. Remote Sens. Environ. 190, 233–246.
Wang, J., Xiao, X., Qin, Y., Doughty, R.B., Dong, J., Zou, Z., 2018. Characterizing the encroachment of juniper forests into sub-humid and semi-arid prairies from 1984 to 2010 using PALSAR and Landsat data. Remote Sens. Environ. 205, 166–179.
Wylie, B.K., Meyer, D.J., Tieszen, L.L., Mannel, S., 2002. Satellite mapping of surface biophysical parameters at the biome scale over the North American grasslands – a case study. Remote Sens. Environ. 79, 266–278.
Xiao, X.M., Boles, S., Liu, J.Y., Zhuang, D.F., Frolking, S., Li, C.S., Salas, W., Moore, B., 2005. Mapping paddy rice agriculture in southern China using multi-temporal MODIS images. Remote Sens. Environ. 95, 480–492.
Xu, D.D., Guo, X.L., 2015. Some insights on grassland health assessment based on remote sensing. Sensors 15, 3070–3089.
Yan, K., Park, T., Yan, G.J., Chen, C., Yang, B., Liu, Z., Nemani, R.R., Knyazikhin, Y., Myneni, R.B., 2016. Evaluation of MODIS LAI/FPAR Product Collection 6. Part 1: consistency and Improvements. Remote Sens.-Basel 8.
Yang, S.X., Feng, Q.S., Liang, T.G., Liu, B.K., Zhang, W.J., Xie, H.J., 2018. Modeling grassland above-ground biomass based on artificial neural network and remote sensing in the Three-River Headwaters Region. Remote Sens. Environ. 204, 448–455.
Yang, Y.H., Fang, J.Y., Pan, Y.D., Ji, C.J., 2009. Aboveground biomass in Tibetan grasslands. J. Arid Environ. 73, 91–95.
Yiran, G.A.B., Kusimi, J.M., Kufogbe, S.K., 2012. A synthesis of remote sensing and local knowledge approaches in land degradation assessment in the Bawku East District, Ghana. Int. J. Appl. Earth Obs. 14, 204–213.
Yu, R., Evans, A.J., Malleson, N., 2018. Quantifying grazing patterns using a new growth function based on MODIS Leaf Area Index. Remote Sens. Environ. 209, 181–194.
Zhang, C.Y., Denka, S., Cooper, H., Mishra, D.R., 2018. Quantification of sawgrass marsh aboveground biomass in the coastal Everglades using object-based ensemble analysis and Landsat data. Remote Sens. Environ. 204, 366–379.
Zhang, X., Friedl, M.A., Tan, B., Goldberg, M.D., Yu, Y., 2012. Long-term detection of global vegetation phenology from satellite instruments, Phenology and climate change. InTech.
Zhang, X.Y., Friedl, M.A., Schaaf, C.B., Strahler, A.H., Hodges, J.C.F., Gao, F., Reed, B.C., Huete, A., 2003. Monitoring vegetation phenology using MODIS. Remote Sens. Environ. 84, 471–475.
Zhou, H., Zhao, X., Tang, Y., Gu, S., Zhou, L., 2005. Alpine grassland degradation and its control in the source region of the Yangtze and Yellow Rivers. China. Grassl. Sci. 51, 191–203.
Zhou, Y.T., Xiao, X.M., Wagle, P., Bajgain, R., Mahan, H., Basara, J.B., Dong, J.W., Qin, Y.W., Zhang, G.L., Luo, Y.Q., Gowda, P.H., Neel, J.P.S., Starks, P.J., Steiner, J.L., 2017. Examining the short-term impacts of diverse management practices on plant phenology and carbon fluxes of Old World bluestems pasture. Agric. For. Meteorol. 237, 60–70.
Zhu, Z., Wang, S.X., Woodcock, C.E., 2015. Improvement and expansion of the Fmask algorithm: cloud, cloud shadow, and snow detection for Landsats 4–7, 8, and Sentinel 2 images. Remote Sens. Environ. 159, 269–277.
Zhu, Z., Woodcock, C.E., 2012. Object-based cloud and cloud shadow detection in Landsat imagery. Remote Sens. Environ. 118, 83–94.